J Biomol NMR (2015) 63:187–199
DOI 10.1007/s10858-015-9974-z

ARTICLE

$^{13}CHD_2$–CEST NMR spectroscopy provides an avenue for studies of conformational exchange in high molecular weight proteins

Enrico Rennella[1] · Rui Huang[1] · Algirdas Velyvis[1] · Lewis E. Kay[1,2]

Received: 23 June 2015 / Accepted: 31 July 2015 / Published online: 14 August 2015

Abstract An NMR experiment for quantifying slow (millisecond) time-scale exchange processes involving the interconversion between visible ground state and invisible, conformationally excited state conformers is presented. The approach exploits chemical exchange saturation transfer (CEST) and makes use of $^{13}CHD_2$ methyl group probes that can be readily incorporated into otherwise highly deuterated proteins. The methodology is validated with an application to a G48A Fyn SH3 domain that exchanges between a folded conformation and a sparsely populated and transiently formed unfolded ensemble. Experiments on a number of different protein systems, including a 360 kDa half-proteasome, establish that the sensitivity of this $^{13}CHD_2$ ^{13}C–CEST technique can be upwards of a factor of 5 times higher than for a previously published $^{13}CH_3$ ^{13}C–CEST approach (Bouvignies and Kay in J Biomol NMR 53:303–310, 2012), suggesting that the methodology will be powerful for studies of conformational exchange in high molecular weight proteins.

Keywords CEST · Methyl-labeling · $^{13}CHD_2$ · Chemical exchange · Proteasome · Sensitivity enhancement

✉ Lewis E. Kay
kay@pound.med.utoronto.ca

[1] Departments of Molecular Genetics, Biochemistry and Chemistry, The University of Toronto, Toronto, ON M5S 1A8, Canada

[2] Program in Molecular Structure and Function, Hospital for Sick Children, 555 University Avenue, Toronto, ON M5G 1X8, Canada

Introduction

The development of powerful isotope labeling schemes has driven many of the important advances in high-resolution NMR studies of biomolecules (Clore and Gronenborn 1991; Goto and Kay 2000; Kainosho et al. 2006; Kay et al. 1990). This includes uniform ^{15}N, ^{13}C labeling of proteins (Ikura et al. 1990) and nucleic acids (Nikonowicz et al. 1992) for studies of dynamics and structure as well as a combination of ^{2}H, ^{15}N, ^{13}C labeling for applications to larger systems (Grzesiek et al. 1993; Yamazaki et al. 1994). Fractional labeling can also be of great utility. One approach that is becoming increasingly popular is the labeling of methyl groups with ^{1}H, ^{13}C in an otherwise uniformly ^{2}H, ^{12}C background (Ayala et al. 2009; Gans et al. 2010; Gardner and Kay 1997; Goto et al. 1999; Isaacson et al. 2007; Tugarinov and Kay 2004; Velyvis et al. 2012). Observation of methyl groups is advantageous since the rapid internal rotation about their three-fold axis leads to narrow lines and facilitates the use of a Transverse Relaxation Optimized Spectroscopy (TROSY) scheme (Tugarinov et al. 2003) that provides an avenue for the study of very high molecular weight protein systems (Rosenzweig and Kay 2014; Ruschak and Kay 2009). In many cases molecular complexes can be studied that are an order of magnitude or more larger than is possible using conventional labeling and spectroscopy (Gelis et al. 2007; Sprangers and Kay 2007).

An attractive feature of the methyl-labeling strategy is that precursors for $^{13}CH_3$-labeling at any methyl position in a protein are now commercially available and methods have been described for 'positioning' methyl groups at key non-methyl containing sites using disulfide chemistry (Religa et al. 2011). Moreover, it is possible to purchase $^{13}CH_2D$ and $^{13}CHD_2$ precursors, and applications using these

isotopomers, in particular in studies of protein dynamics, have appeared (Ishima et al. 1999; Tugarinov and Kay 2005a, b). Not surprisingly, different methyl labeling strategies are optimal depending on the application. For example, we have shown that in structural and functional studies of high molecular weight complexes use of $^{13}CH_3$ isotopomers is advantageous over $^{13}CHD_2$ or $^{13}CH_2D$ (Ollerenshaw et al. 2005; Religa and Kay 2010), largely due to a methyl-TROSY effect that can be exploited, leading to improved resolution and sensitivity. Certain ^{13}C spin-relaxation measurements, however, are best performed on $^{13}CHD_2$ methyl groups (Ishima et al. 1999; Tugarinov and Kay 2005b), as complications from dipolar cross-correlation are largely eliminated. It is envisioned that, in general, many experiments involving the creation of pure ^{13}C magnetization would benefit from the use of singly protonated methyl groups since it is not possible to effect complete transfer of polarization from ^{1}H to ^{13}C in the case of $^{13}CH_2D$ or $^{13}CH_3$ methyls, while in the case of $^{13}CHD_2$ groups this can be achieved in a straightforward manner. One important application involving methyl probes where significant improvements might be possible is CEST (Forsen and Hoffman 1963) whereby sparsely populated, transiently formed ('invisible') states are amplified via detection through the major ('visible') state (Fawzi et al. 2011; Vallurupalli et al. 2012; Zhou and van Zijl 2006). This amplification process occurs over a period of several hundreds of milliseconds during which time individual excited state correlations are selectively perturbed via the application of weak radio frequency fields that affect longitudinal magnetization. Since ^{13}C T_1s are significantly longer for $^{13}CHD_2$ methyl groups relative to $^{13}CH_3$ (one vs three protons) significant sensitivity benefits might be expected in ^{13}C–CEST applications that are optimized for studies of $^{13}CHD_2$-labeled proteins. Finally, since the ^{13}C–^{1}H spin system in a $^{13}CHD_2$ methyl group is effectively 'AX', sensitivity enhancement approaches, leading to the preservation of orthogonal magnetization components that evolve during indirect detection periods, can be utilized (Palmer et al. 1991).

Motivated by the potential benefits described above we have developed a $^{13}CHD_2$ based CEST experiment for studies of conformationally exchanging protein systems and validated the methodology with an application to the G48A Fyn SH3 domain that interconverts between a dominant folded conformer and a sparsely populated unfolded ensemble (Bouvignies et al. 2014). We have compared relative sensitivities in ^{13}C–CEST spectra obtained on a series of [U-^{2}H; Ileδ1-$^{13}CHD_2$; Leu, Val-$^{13}CHD_2$/$^{13}CHD_2$; Met-$^{13}CHD_2$]-labeled proteins and proteins labeled using the 'conventional' approach as [U-^{2}H; Ileδ1-$^{13}CH_3$; Leu, Val-$^{13}CH_3$/$^{12}CD_3$; Met-$^{13}CH_3$] that optimizes signal-to-noise and resolution in HMQC-based ^{13}C–^{1}H correlation spectra of large proteins. Notably, significant sensitivity gains are realized relative to applications using $^{13}CH_3$-labeled proteins and a previously reported $^{13}CH_3$-CEST experiment (Bouvignies and Kay 2012), suggesting that the $^{13}CHD_2$-based CEST methodology can be applied to studies of exchange in high molecular weight complexes. Indeed, CEST spectra recorded on $^{13}CHD_2$ labeled, highly deuterated $\alpha_7\alpha_7$, a 360 kDa half proteasome complex (Sprangers and Kay 2007), are over a factor of five more sensitive than their counterparts recorded on a $^{13}CH_3$-labeled sample.

Materials and methods

Protein sample preparation

All proteins were expressed in *Escherichia Coli* BL21(DE3) cells grown in M9 minimal media (~100 % D_2O), containing ^{15}N-ammonium chloride (1 g/L) and [^{2}H,^{12}C]-glucose (3 g/L) as the nitrogen and carbon sources, respectively. Specifically labeled precursors were added 1 h prior to the induction of protein overexpression with 1 mM IPTG, as described previously (Goto et al. 1999). Purification of samples followed literature protocols. In summary, the following samples were prepared:

1. FF domain from human HYPA/FBP11 (Korzhnev et al. 2010): 1.5 mM [U-^{2}H; Ileδ1-$^{13}CH_3$; Leu, Val-$^{13}CH_3$/$^{12}CD_3$; Met-$^{13}CH_3$]-labeled protein and 1.0 mM [U-^{2}H; Ileδ1-$^{13}CHD_2$; Leu, Val-$^{13}CHD_2$/$^{13}CHD_2$; Met-$^{13}CHD_2$]-labeled protein, 25 mM potassium phosphate, 50 mM NaCl, 1 mM EDTA, 100 % D_2O, pH 6.8.
2. B1 domain of immunoglobulin binding protein G (Huth et al. 1997): 1.5 mM [U-^{2}H; Ileδ1-$^{13}CH_3$; Leu, Val-$^{13}CH_3$/$^{12}CD_3$; Met-$^{13}CH_3$]-labeled protein and 1.0 mM [U-^{2}H; Ileδ1-$^{13}CHD_2$; Leu, Val-$^{13}CHD_2$/$^{13}CHD_2$; Met-$^{13}CHD_2$]-labeled protein, 50 mM potassium phosphate, 100 mM NaCl, 0.1 mM NaN_3, 100 % D_2O, pH 7.5.
3. G48A Fyn SH3 domain (Bouvignies et al. 2014): 1.0 mM [U-^{2}H; Ileδ1-$^{13}CH_3$; Leu, Val-$^{13}CH_3$/$^{12}CD_3$]-labeled protein and 1.35 mM [U-^{2}H; Ileδ1-$^{13}CHD_2$; Leu, Val-$^{13}CHD_2$/$^{13}CHD_2$]-labeled protein, 50 mM sodium phosphate, 0.2 mM EDTA, 0.05 % NaN_3, 10 % D_2O, pH 7.0.
4. The half-proteasome, $\alpha_7\alpha_7$, from *T. Acidophilum* (Sprangers and Kay 2007): 0.9 mM (monomer concentration) samples of [U-^{2}H; Ileδ1-$^{13}CH_3$; Leu, Val-$^{13}CH_3$/$^{12}CD_3$; Met-$^{13}CH_3$]- and [U-^{2}H; Ileδ1-$^{13}CHD_2$; Leu,Val-$^{13}CHD_2$/$^{13}CHD_2$; Met-$^{13}CH_3$]-labeled proteins, 25 mM potassium phosphate, 50 mM NaCl, 0.03 % NaN_3, 1 mM EDTA, 100 % D_2O, pH 7.5.

NMR spectroscopy

All experiments were recorded on a Bruker AVANCE III HD spectrometer equipped with a triple-axis gradient room temperature probe. ^{15}N- and $^{13}CH_3$-based ^{13}C–CEST data sets were recorded as described in the literature (Bouvignies and Kay 2012; Vallurupalli et al. 2012), while $^{13}CHD_2$-based ^{13}C–CEST spectra were measured using the pulse scheme described in the text.

All CEST experiments were recorded as pseudo-3D datasets where each 2D spectrum was obtained as a function of the position of a weak B_1 field that is applied systematically over, in the case of methyl CEST, the methyl ^{13}C spectrum (one plane at a time). For each experiment, two datasets were acquired at B_1 radiofrequency field strengths of 25 and 40 Hz. The B_1 field was calibrated through a nutation experiment, as described previously (Guenneugues et al. 1999). For the $^{13}CHD_2$–CEST experiments the position of the B_1 field ranged from 8.3 to 26.8 ppm, uniformly sampled in 114 (25 Hz) and 72 (40 Hz) steps, for net measurement times of 32.5 and 20.5 h, respectively. ^{15}N CEST experiments were recorded to cross-validate the exchange parameters obtained from fits of the ^{13}C–CEST profiles. Here the position of the weak B_1 field varied between 105.3 and 134.9 ppm, uniformly sampled in 74 (25 Hz) and 47 (40 Hz) steps, with net measurement times of 28 and 18 h, respectively. T_{MIX} was set to 0.5 s in all CEST experiments.

^{1}H longitudinal relaxation rate constants were measured by dephasing the initial ^{1}H magnetization through a combination of rf purge and ^{1}H 90°-pulsed field gradient elements. After a subsequent relaxation delay, spectra were recorded using a standard ^{1}H–^{13}C HSQC pulse sequence. The relaxation delays used were 0.001, 0.05, 0.1, 0.15, 0.2, 0.3, 0.4, 0.5, 0.7 and 0.9 s. ^{13}C R_1 values for $^{13}CHD_2$ labeled protein samples were measured with a modified version of the CEST scheme presented here, by first removing the ^{13}C CW element during T_{MIX}. A series of spectra were recorded with T_{MIX} delays of 0.005, 0.05, 0.1, 0.15, 0.2, 0.3, 0.4, 0.5 s. A similar approach was taken for $^{13}CH_3$ labeled samples except that a modified $^{13}CH_3$-based ^{13}C–CEST scheme was used. ^{1}H and ^{13}C rate constants were obtained by fitting peak intensities to single exponential decay functions, $y = A\exp(-R_1 T_{MIX})$, recognizing that this analysis does not take into account cross-correlated relaxation effects (see below) nor cross-relaxation with neighboring proton spins from adjacent methyls.

In order to compare the signal-to-noise (s/n) values for $^{13}CH_3$- and $^{13}CHD_2$-based CEST experiments it is critical that the relative concentrations of the [U-^{2}H; Ileδ1-$^{13}CH_3$; Leu, Val-$^{13}CH_3$/$^{12}CD_3$; Met-$^{13}CH_3$]- and [U-^{2}H; Ileδ1-$^{13}CHD_2$; Leu, Val-$^{13}CHD_2$/$^{13}CHD_2$; Met-$^{13}CHD_2$]-labeled samples be known. For all proteins, with the exception of $\alpha_7\alpha_7$, this was achieved by recording ^{1}H–^{15}N correlation maps for each sample and calculating relative intensities of corresponding peaks in each data set. The relative concentration was then obtained as:

$$\sum_i \frac{I_{CHD_2,i}}{I_{CH_3,i}}$$

where the sum is over all ratios of corresponding cross-peaks in the data sets of the $^{13}CH_3$ and $^{13}CHD_2$ labeled samples. In the case of $\alpha_7\alpha_7$ intensities of Met methyl correlations have been directly compared in samples to estimate the relative concentrations (note that Met in both ILV-$^{13}CHD_2$ and ILV-$^{13}CH_3$ samples is of the $^{13}CH_3$ variety so that a direct comparison is possible). All s/n values reported in the text were normalized by concentration ratios calculated as described.

Data analysis

All ^{15}N and $^{13}CHD_2$-(with ^{2}H decoupling) CEST data were fit to a two-state model of chemical exchange, $G \underset{k_{EG}}{\overset{k_{GE}}{\rightleftarrows}} E$, as described in detail previously (Vallurupalli et al. 2012). The fitting parameters are ($k_{ex} = k_{GE} + k_{EG}$, p_E, ω_G, ω_E, R_1^G, R_2^G, R_2^E, I_0), where p_E is the fractional population of the excited state, $\omega_{E(G)}$ is the chemical shift of the excited (ground) state spin, R_i^j is the longitudinal ($i = 1$) or transverse ($i = 2$) relaxation rate of the spin in state $j \in (G, E)$ and I_0 is the cross-peak intensity in the spectrum recorded with $T_{MIX} = 0$ s; R_1^G, R_2^G, R_2^E and I_0 are residue specific parameters. Prior to analysis of the $^{13}CHD_2$ (^{2}H decoupling) data, dips corresponding to ^{2}H decoupling sidebands were eliminated from profiles by removing experimental points in the range ±(^{2}H decoupling field strength ±50) Hz from the major state dip, corresponding to ±(450–550) Hz in the present set of applications where a 500 Hz decoupling field was used.

$^{13}CHD_2$-based ^{13}C CEST data acquired without ^{2}H decoupling during T_{MIX} were fit to a two-state model of exchange using a more complex exchange matrix that takes into account the spin states of the pair of ^{2}H spins that are coupled to ^{13}C, as described in detail in the "Appendix". The fitting parameters are (k_{ex}, p_E, ω_G, ω_E, R_1^G, R_2^G, R_2^E, I_0, κ_1, κ_2, $^1J_{CD}$), where κ_1 and κ_2 are ^{2}H relaxation terms and $^1J_{CD}$ is the one bond ^{13}C–^{2}H scalar coupling constant.

Results and discussion

CEST spectroscopy as a probe of conformational dynamics

The basic CEST experiment involves recording a series of data sets in which the position of a weak (~10–50 Hz) radio frequency (rf) pulse, applied during an interval where

the magnetization of interest is longitudinal, is varied from one spectrum to the next (Fawzi et al. 2011; Vallurupalli et al. 2012; Zhou and van Zijl 2006). When the rf field is positioned at the resonance frequency of a peak from the excited state (typically invisible in most applications) its longitudinal magnetization is decreased from the equilibrium value. The resulting perturbation is then transferred via chemical exchange to the major state (visible) correlation where it is detected as a decrease in the intensity of the observed cross-peak. Correspondingly, spins in the major state become saturated when the rf field is applied on resonance so that a plot of the intensity of an observed correlation as a function of the position of the rf field gives a CEST profile with a pair of dips corresponding to the positions of resonances in the major and minor states. Because the rf field is applied for several hundreds of milliseconds the longitudinal relaxation properties of spin probes are critical for sensitivity. Additionally, as in all NMR experiments, longitudinal relaxation rates of the starting polarization also play an important role in dictating the resulting sensitivity of the experiment. Therefore, we performed initial ^{13}C and ^{1}H longitudinal relaxation measurements on a number of $^{13}CH_3$- and $^{13}CHD_2$-labeled protein samples to evaluate what the implications of the relaxation rates might be for the sensitivity of the methyl-CEST experiment using these different labeling schemes.

^{1}H and ^{13}C methyl spin–lattice relaxation rates are highly correlated and very similar

Figure 1 shows plots of ^{13}C (open symbols) and ^{1}H (filled) R_1 rates for $^{13}CH_3$ (red) and $^{13}CHD_2$ (blue) methyl groups in the FF domain from human HYPA/FBP11, 25 °C (a, b), the B1 domain of immunoglobulin binding protein G (GB1), 25 °C (c, d), and for the G48A Fyn SH3 domain at 25 °C (e, f) and 5 °C (g, h). Two major points emerge. First, R_1^C and R_1^H values for a given methyl group are very similar (compare red open, closed or blue open, closed) and second R_1 rates are significantly higher for $^{13}CH_3$ than for $^{13}CHD_2$ methyl groups (red vs blue), by factors of approximately 2.1 and 2.3 for ^{1}H and ^{13}C, respectively. This has implications for the relative sensitivities of $^{13}CH_3$ versus $^{13}CHD_2$ CEST experiments and notably the combined effects of ^{1}H and ^{13}C rates tend to cancel to a significant extent. For example, larger R_1^H rates for $^{13}CH_3$ methyl groups lead to an increase in the s/n per unit measurement time since methyl proton polarization recovers more completely between scans, yet the corresponding increase in R_1^C rates is deleterious since the ^{13}C–CEST effect occurs optimally when participating ^{13}C spins have slow longitudinal relaxation rates.

A straightforward calculation shows why the correlation between R_1^C and R_1^H is so high. In what follows we consider a $^{13}CHD_2$ methyl group initially and focus only on the dominant relaxation contributions from ^{1}H–^{13}C dipolar interactions, although the conclusions hold if additional terms from less significant relaxation effects are included. Then R_1^C and R_1^H are given by (Abragam 1961)

$$R_1^C = \frac{1}{10}\frac{\gamma_H^2\gamma_C^2\hbar^2}{r_{HC}^6}\left(J(\omega_H-\omega_C)+3J(\omega_C)+6J(\omega_H+\omega_C)\right)$$
$$R_1^H = \frac{1}{10}\frac{\gamma_H^2\gamma_C^2\hbar^2}{r_{HC}^6}\left(J(\omega_H-\omega_C)+3J(\omega_H)+6J(\omega_H+\omega_C)\right) \quad (1)$$

where γ_j is the gyromagnetic ratio of spin j, $\hbar$ is Planck's constant divided by 2π, r_{HC} is the length of the ^{1}H–^{13}C bond and $J(\omega)$ is the spectral density function defined as (Lipari and Szabo 1982)

$$J(\omega) = \frac{\frac{1}{9}S_{axis}^2\tau_M}{1+(\omega\tau_M)^2} + \frac{\left(1-\frac{1}{9}S_{axis}^2\right)\tau_e}{1+(\omega\tau_e)^2}, \quad \frac{1}{\tau_e} = \frac{1}{\tau_M} + \frac{1}{\tau_I} \quad (2)$$

where τ_M is the assumed isotropic tumbling time, τ_I is the correlation time for the rapid rotation about the methyl three-fold axis, S_{axis}^2 is the square of an order parameter that quantifies the amplitude of the methyl axis motion and the factor of 1/9 takes into account the orientation of the methyl ^{1}H–^{13}C bond vector with respect to the three-fold axis. If $R_1^C \approx R_1^H$ then it follows that $J(\omega_C) \approx J(\omega_H)$ (Eq. 1) and the second term in the spectral density of Eq. (2) must contribute to R_1 much more than the first. Indeed, a straightforward calculation with $\tau_M = 5$ ns, $\tau_I = 30$ ps and $S_{axis}^2 = 0.5$ establishes that the τ_M term in Eq. (2) contributes less than 15 % to R_1^C (600 MHz ^{1}H frequency) and much less to R_1^H and further as τ_M increases the contribution becomes even less significant. Thus,

$$R_1^C \approx R_1^H \approx \frac{\gamma_H^2\gamma_C^2\hbar^2}{r_{HC}^6}\left(\left(1-\frac{1}{9}S_{axis}^2\right)\tau_I\right). \quad (3)$$

A similar scenario exists for a $^{13}CH_3$-labeled methyl group. In this case the ^{1}H–^{13}C dipolar interactions dominate R_1^C (contributions >95 % for the dynamics parameters considered above) although for R_1^H the geminal ^{1}H–^{1}H dipolar interactions contribute more than do ^{1}H–^{13}C interactions (ratio of ~7:3). Neglecting cross-correlation it can be shown that

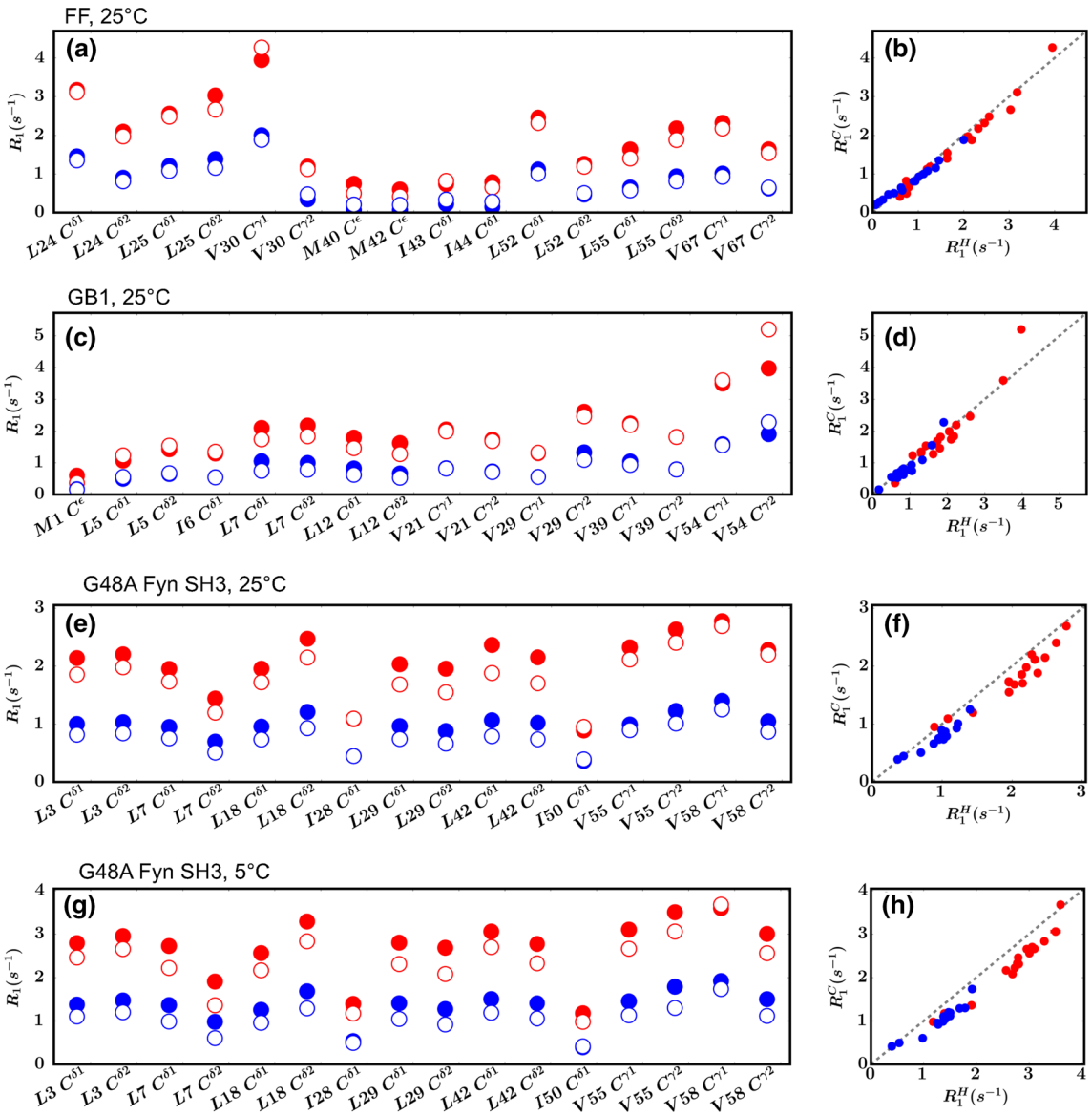

Fig. 1 ^{1}H and ^{13}C R_1 relaxation rates for $^{13}CH_3$ (*red symbols*) and $^{13}CHD_2$ (*blue*) methyl groups measured on [U-^{2}H; Ileδ1-$^{13}CH_3$; Leu, Val-$^{13}CH_3$/$^{12}CD_3$; Met-$^{13}CH_3$]- and [U-^{2}H; Ileδ1-$^{13}CHD_2$; Leu, Val-$^{13}CHD_2$/$^{13}CHD_2$; Met-$^{13}CHD_2$]-labeled samples. R_1 values measured for the FF domain from human HYPA/FBP11, 25 °C (**a**), for the B1 domain of immunoglobulin binding protein G (GB1), 25 °C (**c**) and for the G48A Fyn SH3 domain at 25 °C (**e**) and 5 °C (**g**) are shown. In (**a**, **c**, **e**, **g**) the *open* and *closed symbols* denote ^{13}C and ^{1}H rates, respectively, with each methyl group listed along the x-axis. In (**b**, **d**, **f**, **h**) linear correlation plots of R_1^C versus R_1^H are presented. *Error bars* for relaxation rates are included, but are significantly smaller than the symbols

$$
\begin{aligned}
R_1^C &\approx \frac{3\gamma_H^2\gamma_C^2\hbar^2}{r_{HC}^6}\left(\left(1-\frac{1}{9}S_{axis}^2\right)\tau_I\right)\\
R_1^H &\approx \frac{\gamma_H^2\gamma_C^2\hbar^2}{r_{HC}^6}\left(\left(1-\frac{1}{9}S_{axis}^2\right)\tau_I\right)\\
&\quad+\frac{3\gamma_H^4\hbar^2}{r_{HH}^6}\left(\left(1-\frac{1}{4}S_{axis}^2\right)\tau_I\right)
\end{aligned}
\tag{4}
$$

where $\frac{R_1^H}{R_1^C}$ varies from 1.18 to 1.03 for S_{axis}^2 between 0 and 1, assuming $r_{HC} = 1.095$ Å and $r_{HH} = 1.78$ Å. Thus, to excellent approximation $R_1^C \approx R_1^H$ in this case as well. A more detailed calculation shows that for R_1^C and R_1^H the effects of both ^{1}H–^{13}C and ^{1}H–^{1}H cross-correlated relaxation are very small in the limit that methyl rotation is the dominant contributor to relaxation (Kay and Torchia 1991; Werbelow and Grant 1977; Werbelow and Marshall 1973) so that the arguments above hold in the general case.

In order to explore the trade-off in spectral signal from the interplay between R_1^C and R_1^H we have calculated

relative signal intensities for corresponding peaks in $^{13}CHD_2$ and $^{13}CH_3$ CEST experiments considering only R_1 relaxation and assuming equivalent recycle delays in each case, Fig. 2. In this case the signal intensity is given by the relation,

$$Signal = (1 - \exp(-R_1^H T_{RD}))\exp(-R_1^C T_{MIX}) \quad (5)$$

where T_{RD} is the recycle delay, T_{MIX} is the CEST delay during which the weak perturbing rf field is applied and the experimentally derived R_1 values for the G48A Fyn SH3 domain (25 °C) have been used. For $T_{MIX} > 0.25$ s and $T_{RD} \geq 1.5$ s, that are typically used in most CEST studies, notable gains are achieved for the $^{13}CHD_2$ labeling approach, but the compensation effect between R_1^C and R_1^H means that they are not as large as might be expected if only relaxation during the T_{MIX} period is considered.

As a final note it is worth mentioning that the near independence of R_1^H on tumbling time has important implications for the use of methyl probes in NMR studies of macromolecules in general. Because R_1^H is only marginally affected by τ_M, the steady state ^1H magnetization at the start of each scan in a ^1H–^{13}C correlation experiment will not be affected adversely by molecular size or by static magnetic field. In contrast, in the case of highly deuterated proteins the amide ^1H R_1 rates decrease significantly with increasing molecular size or field, leading to a net decrease in experimental sensitivity.

A pulse scheme for $^{13}CHD_2$–CEST

Figure 3 shows the sequence that has been developed for studies of slow conformational dynamics using $^{13}CHD_2$ methyl group probes with the basic flow of magnetization summarized succinctly as

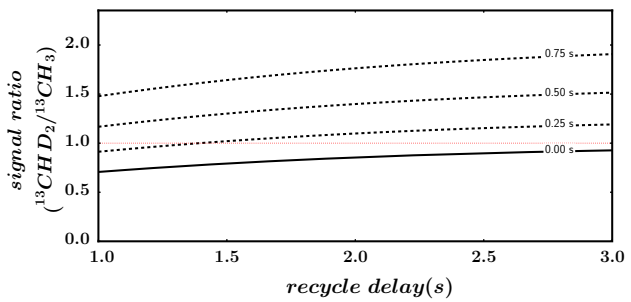

Fig. 2 Comparative intensities of correlations in $^{13}CHD_2$- versus $^{13}CH_3$-CEST spectra, including *only* contributions from longitudinal relaxation, as a function of the recycle (T_{RD}) and CEST (T_{MIX}) relaxation delays. The signal in each data set is calculated according to Eq. (5) of the text. Signal ratio profiles are obtained for each residue of the G48A Fyn SH3 domain (25 °C) using experimentally derived R_1 values and subsequently averaged to produce the curves shown in the figure

$$^1H \xrightarrow{J_{CH}} {}^{13}C(CEST, T_{MIX}) \longrightarrow {}^{13}C(t_1) \xrightarrow{J_{CH}} {}^1H(t_2) \quad (6)$$

Briefly, initial ^1H polarization is transferred via a refocused INEPT element to ^{13}C Z magnetization and subsequently a weak ^{13}C rf field is applied for a duration T_{MIX} during which time CEST occurs. In order to collapse the multiplet components that would otherwise manifest from ^1H–^{13}C scalar coupling, a $90_x240_y90_x$ ^1H decoupling element (Levitt 1982) is applied during T_{MIX}, as described previously (Vallurupalli et al. 2012). During this interval ^2H continuous wave decoupling can also be applied to narrow the dips in the resulting CEST profiles that otherwise would be broadened from one bond ^{13}C–^2H scalar couplings and ^2H spin flips that interconvert magnetization between unresolved ^{13}C–^2H multiplet components. ^{13}C chemical shift is recorded at the completion of the CEST element and then both quadrature components transferred back to ^1H for observation using a planar-TOCSY scheme (Sattler et al. 1999). It is noteworthy that ^1H WALTZ decoupling (Shaka et al. 1983) commences $t_1^{MAX} - t_1$ prior to the t_1 period, so that decoupling is applied for a net time of t_1^{MAX}, where t_1^{MAX} is the maximum t_1 acquisition time. This ensures that heating is independent of the duration of t_1, eliminating potential distortions in lineshapes (Wang and Bax 1993). A series of 2D data sets are recorded, each with the ^{13}C rf field applied at a different position during T_{MIX}, and the intensities of each of the resulting cross-peaks plotted as a function of the rf offset to generate CEST profiles that can be subsequently analyzed to extract exchange parameters as well as the methyl ^{13}C chemical shifts of the excited state.

As described above, ^2H decoupling is applied during T_{MIX} to eliminate the effects of ^2H spin flips that typically are on a similar time-scale as $1/J_{CD}$, where J_{CD} is the one-bond ^{13}C–^2H scalar coupling constant. Here we have used a 0.5 kHz continuous wave field that is easily accommodated on our Bruker AVANCE III HD spectrometer. However, on other spectrometer systems it may not be possible to apply ^2H rf for a duration T_{MIX} that can extend to many hundreds of milliseconds. In this case ^2H decoupling is not used, and the effects of ^2H spin-flips must be taken into account in the analysis of CEST profiles since they typically occur with rates that are similar to the kinetics of interconversion between conformational states. Equations describing the evolution of magnetization in a $^{13}CHD_2$ methyl group from ^2H spin-flips are provided in the "Appendix".

Comparison of $^{13}CHD_2$- and $^{13}CH_3$-CEST

$^{13}CHD_2$–CEST data sets have been recorded on a G48A Fyn SH3 domain sample that has been shown previously to interconvert between folded and unfolded conformers with

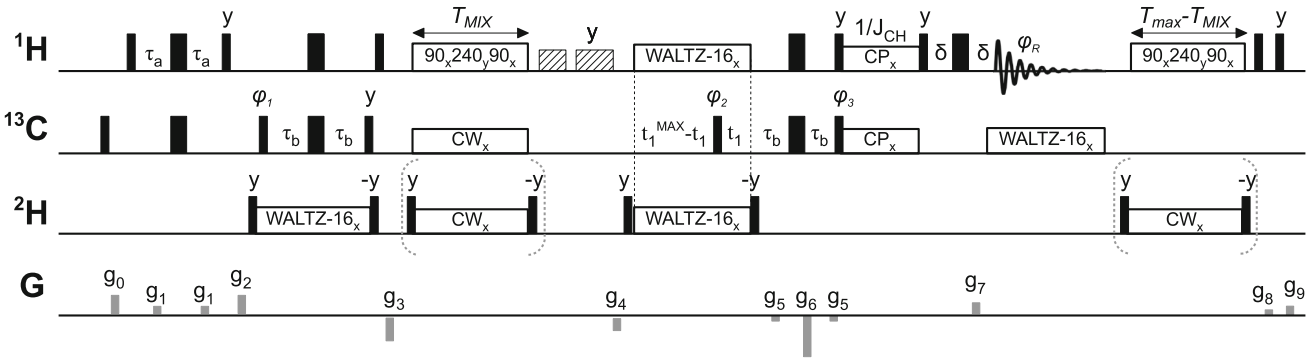

Fig. 3 Pulse scheme of the ^{13}C-methyl CEST experiment for $^{13}CHD_2$-labeled proteins. *Narrow* and *wide black bars* denote 90° and 180° pulses, respectively, applied at maximum power and along the x-axis unless otherwise indicated. ^{1}H, ^{2}H and ^{13}C transmitters are positioned in the center of the methyl region except during acquisition (t_2) when the ^{1}H carrier is placed on water and during T_{MIX} when the ^{13}C transmitter is positioned at the desired offset for weak irradiation (denoted by CW, typically 15–50 Hz). During T_{MIX} ^{1}H decoupling is achieved using a 3.6 kHz $90_x240_y90_x$ (Levitt 1982) decoupling field as discussed previously (Vallurupalli et al. 2012), while heteronuclear cross-polarization denoted by CP (duration ~8 ms) is achieved with an 8 kHz DIPSI-2 field (Shaka et al. 1988) applied to both ^{1}H and ^{13}C. Water suppression is accomplished, in part, using purge elements (3.6 kHz) of durations 2 (x-axis) and 3.4 ms (y-axis) (Messerlie et al. 1989), indicated by *striped boxes*, and a 6.25 kHz WALTZ-16 field (Shaka et al. 1983) is used for ^{1}H decoupling during t_1. ^{2}H decoupling is applied during T_{MIX} via a 500 Hz continuous wave field, flanked by 1.9 kHz ^{2}H pulses, and during t_1 using a 710 Hz WALTZ-16 field. Although experiments can be recorded with or without ^{2}H decoupling during T_{MIX} (hence parenthesis) we recommend the former. Typically 50–100 2D data sets are recorded for each CEST experiment, including a reference spectrum with $T_{MIX} = 0$; in this case a ^{1}H $90_x240_y90_x$ element is applied after acquisition so that the average heating in each data set is similar. The following phase cycle is used: φ_1 = x, −x; φ_2 = y, y, −y, −y; φ_3 = y; φ_R = x, −x, −x, x. Quadrature detection in the indirect dimension is obtained using the gradient enhanced sensitivity approach (Kay et al. 1992; Schleucher et al. 1993) whereby separate data sets are recorded for each t_1 point with (φ_3, g_6) and ($-\varphi_3$, $-g_6$). The delays used are: $\tau_a = 1.8$ ms, $\tau_b = 2$ ms, t_1^{MAX} = maximum t_1 delay value, $\delta = 460$ µs, recycle delay ~2 s. Gradients are applied with the following durations (ms) and strengths (G/cm): g_0: (1, 21.4), g_1:(0.5, 16); g_2: (0.8, 26.8); g_3: (1, −26.8); g_4: (0.9, −16); g_5: (0.3, −21.4); g_6: (1.02, −48.2); g_7: (0.26, 48.2); g_8: (0.22, −16); g_9: (0.45, −16). The g_5 gradient pair is inverted with g_6

a rate constant of approximately 100 s^{-1}, 25 °C (Bouvignies et al. 2014). A pair of data sets with weak ^{13}C rf fields of 25 and 40 Hz were obtained. Figure 4a shows a region of the ^{13}C–^{1}H correlation map measured with the pulse scheme of Fig. 3, $T_{MIX} = 0$ (blue), superimposed on a $T_{MIX} = 0$ plane (red) from a $^{13}CH_3$-CEST data set recorded on a [U-^{2}H; Ileδ1-$^{13}CH_3$; Leu, Val-$^{13}CH_3$/$^{13}CD_3$; Met-$^{13}CH_3$] sample. Figure 4b compares the intensities of the Leu 29 $C^{\delta 2}$-$H^{\delta 2}$ correlation from spectra recorded on the $^{13}CHD_2$ (blue) and $^{13}CH_3$ (red) samples using $T_{MIX} = 0$ s (solid lines) and 500 ms (dotted lines), 25 °C, with a similar comparison in Fig. 4c for data recorded at 5 °C. In all cases spectral intensities have been adjusted to take into account small differences in protein concentrations and the fact that the noise floor in the $^{13}CHD_2$–CEST is $\sqrt{2}$ higher than in the $^{13}CH_3$-CEST (due to the enhanced sensitivity scheme of Fig. 3). We have further quantified the sensitivity gains on a per-residue basis, as shown in Figure d (25 °C) and e (5 °C), where s/n ratios from spectra recorded with the scheme of Fig. 3 and $^{13}CHD_2$ labeled protein and from $^{13}CH_3$-CEST experiments (Bouvignies and Kay 2012) recorded on a $^{13}CH_3$-labeled sample are presented. When $T_{MIX} = 0$ ($\tau_M \sim 3$ ns, 25 °C) the average s/n ratio, r, for Leu/Val methyl groups is 2.0 ± 0.1 in favor of $^{13}CHD_2$ labeling (ranging from 1.4 to 2.5) that increases to 3.6 ± 0.2 (2.4–5.6) for $T_{MIX} = 0.5$ s. Even larger enhancements are observed at 5 °C ($\tau_M \sim 6$ ns) where $r = 3.0 \pm 0.1$ (2.3–4.4) and 6.3 ± 0.5 (4.4–10.7) for $T_{MIX} = 0$ and 0.5 s, respectively. Figure 4d and e show that the gains for Ile residues are typically half those for Leu/Val since the effective concentration of 'NMR active' methyl groups is the same for Ile using the $^{13}CH_3$ and $^{13}CHD_2$-labeling strategies described in Materials and Methods (see below). Finally, it is important to emphasize that for each application the relevant s/n gain of one method over the other must be evaluated for the T_{MIX} used. We have included values for $T_{MIX} = 0$ above as a baseline because they represent the minimum expected sensitivity gain (see below).

The substantial gains associated with the use of [U-^{2}H; Ileδ1-$^{13}CHD_2$; Leu, Val-$^{13}CHD_2$/$^{13}CHD_2$; Met-$^{13}CHD_2$]-labeled proteins as opposed to the more standard [U-^{2}H; Ileδ1-$^{13}CH_3$; Leu, Val-$^{13}CH_3$/$^{12}CD_3$; Met-$^{13}CH_3$]-labeling for methyl CEST derive from a number of factors. First, every Leu/Val methyl group is $^{13}CHD_2$ labeled, while only 1 in 2 is NMR active when the $^{13}CH_3$ isotopomer is used. Labeling one of every two isopropyl methyls in Leu/Val with $^{13}CH_3$ (the other is $^{12}CD_3$) minimizes the proton density in the protein, resulting in higher sensitivity and resolution in studies of high molecular weight protein

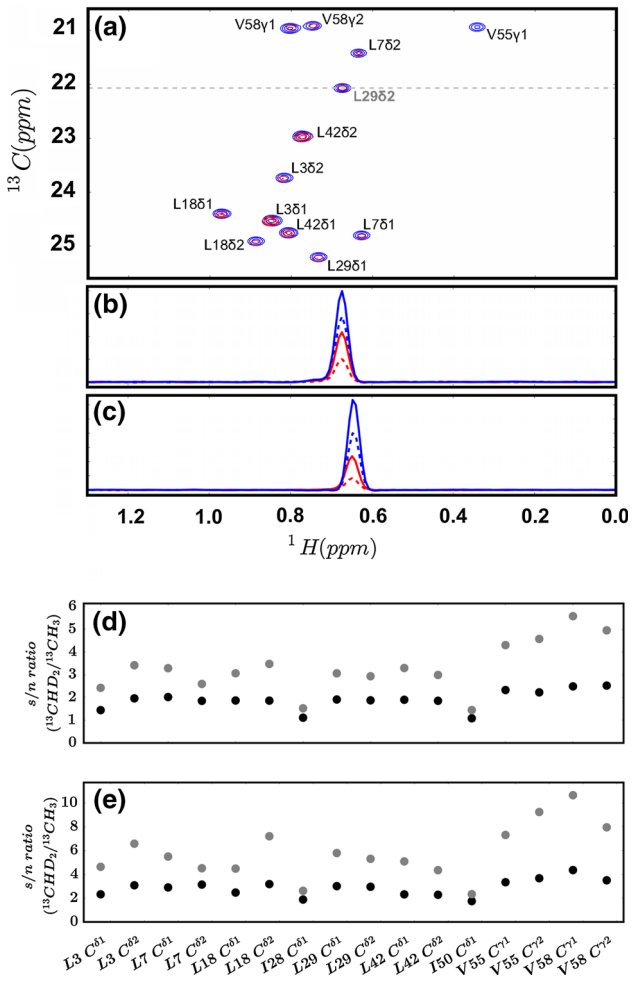

Fig. 4 **a** Superposition of selected regions from ^{13}C–^{1}H correlation maps of [U-^{2}H; Ileδ1-$^{13}CH_3$; Leu, Val-$^{13}CH_3/^{12}CD_3$]- and [U-^{2}H; Ileδ1-$^{13}CHD_2$; Leu, Val-$^{13}CHD_2/^{13}CHD_2$]-labeled G48A Fyn SH3 domains, 25 °C, 600 MHz (^{1}H frequency) recorded using $^{13}CH_3$- (*red*) (Bouvignies and Kay 2012) and $^{13}CHD_2$- (*blue*) CEST based pulse schemes, $T_{MIX} = 0$ s. The chemical shift coordinates for the spectrum of the $^{13}CH_3$ sample have been adjusted to account for ^{2}H isotope effects. **b**, **c** Cross-sections at 23 ppm (*dashed line*) for Leu29 $C^{\delta 2}$-$H^{\delta 2}$ are plotted in **b**, 25 °C and **c**, 5 °C (*blue* $^{13}CHD_2$; *red* $^{13}CH_3$; *continuous lines* $T_{MIX} = 0$ s; *dashed lines* $T_{MIX} = 0.5$ s), normalized to take into account small differences in protein concentrations and the $\sqrt{2}$ increase in the noise floor of $^{13}CHD_2$–CEST spectra. **d**, **e** Relative s/n ratios of cross-peaks ($^{13}CHD_2/^{13}CH_3$) in CEST spectra recorded with $T_{MIX} = 0$ s (*black circles*) and $T_{MIX} = 0.5$ s (*grey*), 25 °C (**d**) and 5 °C (**e**). Data were acquired with a recycle delay of 1.9 s; only a small change in relative intensities of cross-peaks in favor of the $^{13}CH_3$ experiment was observed using a recycle delay of 1.5 s. *Error bars* in **d** and **e** are included, but are significantly smaller than the symbols

systems that make use of the methyl-TROSY effect (Tugarinov and Kay 2004). The labeling approach may not be optimal, however, in HSQC-based applications where the TROSY effect cannot be exploited and where in-phase ^{13}C magnetization is required. As discussed in detail previously, the requirement for the creation of longitudinal ^{13}C magnetization decreases the sensitivity of the $^{13}CH_3$-CEST experiment approximately three-fold relative to a standard HSQC (Bouvignies and Kay 2012). In contrast, no such sensitivity loss is present in $^{13}CHD_2$–CEST since the transfer from ^{1}H to ^{13}C is complete in the case of AX spin systems. Thus, considering only the 'nature of the spin systems' and neglecting relaxation, similar s/n values would be expected from $^{13}CHD_2$ and $^{13}CH_3$ methyl groups in methyl-CEST spectra. A further advantage of the $^{13}CHD_2$ labeling scheme emerges from the fact that it is possible to preserve both quadrature t_1 components, leading to a maximum increase in s/n of 1.4 (Palmer et al. 1991). As illustrated in Fig. 4d, the sensitivity advantages for the $^{13}CHD_2$–CEST approach increase with T_{MIX} because of the longer ^{13}C R_1 rates in $^{13}CHD_2$ methyl groups (compare grey vs black) and applications to systems with particularly slow exchange rates will show large benefits. Moreover, ^{13}C and ^{1}H transverse relaxation rates tend to be more favorable in $^{13}CHD_2$ methyl groups then in $^{13}CH_3$ methyls in the absence of the methyl-TROSY effect, leading to a decrease in transverse relaxation losses during the course of the pulse scheme in the case of $^{13}CHD_2$-labeling. As noted above, the slower longitudinal ^{1}H relaxation rates for $^{13}CHD_2$ relative to $^{13}CH_3$ do lead to a sensitivity loss in the case of $^{13}CHD_2$-labeling but this is more than offset, in general, by the gain from the longer ^{13}C longitudinal relation times. Finally, additional gains in s/n in favor of $^{13}CHD_2$-labeling are further noted as the temperature decreases (Fig. 4e). This is due to increased relaxation rates (both longitudinal and transverse) for ^{13}C and ^{1}H magnetization in $^{13}CH_3$- relative to $^{13}CHD_2$ methyl groups, leading to more significant decreases in sensitivity for CEST-spectra recorded with $^{13}CH_3$ probes.

Validation of the methodology

Figure 5 shows representative CEST profiles recorded on a sample of [U-^{2}H; Ileδ1-$^{13}CHD_2$; Leu, Val-$^{13}CHD_2/^{13}CHD_2$]-labeled G48A Fyn SH3 domain, 25 °C using the scheme of Fig. 3, with (green) and without (blue) ^{2}H continuous wave decoupling during the CEST period. Global fits of all CEST profiles simultaneously are shown with solid lines. Notably, weak sidebands are observed when ^{2}H decoupling is applied, positioned $\pm B_1$ Hz from the dip associated with the major state, where B_1 is the strength of the ^{2}H decoupling field. The dips associated with these sidebands lie well outside the region where minor state resonance positions are expected (typically within 2 ppm of the major dip) and 'contaminated' points can be removed prior to fitting the profiles to extract the exchange parameters. The line-narrowing that results from ^{2}H decoupling can be observed for a number of the profiles, in particular for L42-$C^{\delta 2}$, but the effect is relatively small

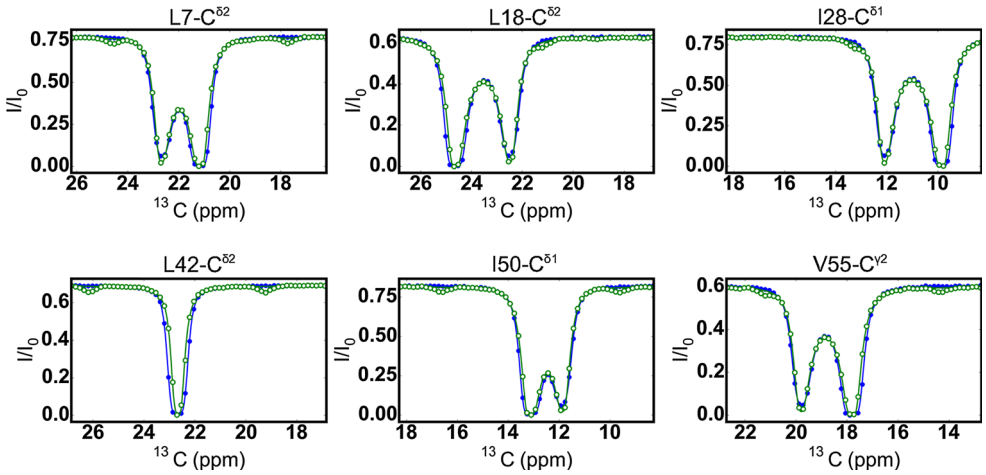

Fig. 5 Representative CEST profiles recorded on a [U-^{2}H; Ileδ1-^{13}CHD$_2$; Leu, Val-^{13}CHD$_2$/^{13}CHD$_2$]-labeled sample of the G48A Fyn SH3 domain, 25 °C, 600 MHz. Data sets were measured with the scheme of Fig. 3, $T_{MIX} = 0.5$ s and a weak B_1 field strength of 25 Hz, without (*blue filled circles*) or with (*green open circles*) deuterium decoupling during T_{MIX}. *Continuous lines* are the fitted profiles to a model of two-site chemical exchange. Note the small decoupling sidebands separated by 500 Hz from the major state dip in the case of profiles recorded with ^{2}H decoupling; points arising from the sidebands are removed prior to fitting

since the dips are 'artificially broadened' by the B_1 field that is used (25 Hz in this case). The effects of ^{2}H decoupling are much more than cosmetic, however. We were unable to properly fit CEST profiles recorded without decoupling using a simple formalism that did not take into account ^{2}H spin flips but assumed that each dip was a composite of multiplet components in the ratio 1:2:3:2:1 (Vallurupalli and Kay 2013). In general, a more elaborate analysis of the data is required in the absence of ^{2}H decoupling, as described in the "Appendix". We prefer, therefore, to use ^{2}H decoupling where possible, especially since the required decoupling field is not prohibitive.

^{13}CHD$_2$–CEST profiles recorded using rf fields of 25 and 40 Hz were fit globally to a two-state model of chemical exchange, $G \underset{k_{EG}}{\overset{k_{GE}}{\rightleftarrows}} E$, to extract the population of the excited state, p_E and $k_{ex} = k_{EG} + k_{GE}$. Figure 6a shows the distribution of (p_E, k_{ex}) values from fits of the data recorded without [blue, (p_E, k_{ex}) = (9.3 ± 0.1 %, 101 ± 2 s^{-1})] and with [green, (p_E, k_{ex}) = (9.5 ± 0.1 %, 105 ± 2 s^{-1})] ^{2}H decoupling. In order to cross-validate the parameters, we have recorded an ^{15}N-CEST data set, as described previously (Vallurupalli et al. 2012), with (p_E, k_{ex}) = (9.2 ± 0.1 %, 109 ± 2 s^{-1}) that is in excellent agreement with the fitted parameters from the methyl data. Figure 6b compares extracted chemical shift differences between corresponding nuclei in ground and excited states as measured from ^{13}CHD$_2$–CEST with previously published values obtained from ^{13}CH$_3$-CEST (Bouvignies and Kay 2012) and, as expected, the agreement is excellent.

High sensitivity gains are obtained in studies of a 360 kDa complex

As a final example we have compared s/n values in ^{13}C–CEST data sets recorded on samples of ^{13}CHD$_2$- and ^{13}CH$_3$-labeled $\alpha_7\alpha_7$. The $\alpha_7\alpha_7$ complex can be thought of as a 'half-proteasome', comprising two of the four heptameric rings that are arranged axially in the full proteasome, $\alpha_7\beta_7\beta_7\alpha_7$ (Lowe et al. 1995). Figure 7a illustrates a region of the ^{13}C–^{1}H correlation map of [U-^{2}H; Ileδ1-^{13}CHD$_2$; Leu, Val-^{13}CHD$_2$/^{13}CHD$_2$; Met-^{13}CH$_3$]-$\alpha_7\alpha_7$ recorded using the pulse scheme of Fig. 3 with $T_{MIX} = 0$ s, 50 °C. Figure 7b compares s/n ratios for cross-peaks in ^{13}CHD$_2$- versus ^{13}CH$_3$-CEST, showing significant sensitivity advantages for the ^{13}CHD$_2$-based experiment, $r = 3.5 \pm 0.1$ (2.8–4.7) for $T_{MIX} = 0$ s and $r = 6.5 \pm 0.4$ (3.2–15.3) for $T_{MIX} = 0.5$ s in the case of Leu/Val methyl groups. As expect sensitivity gains for Ile are approximately half those for Leu/Val, $r = 3.8 \pm 0.2$ (3.1–5.4) for $T_{MIX} = 0.5$ s

Concluding remarks

We have described a ^{13}CHD$_2$-based CEST pulse scheme for studies of millisecond time-scale exchange processes in proteins. The utility of the method has been demonstrated with an application to a G48A Fyn SH3 domain that exchanges between the major state native conformation and a second low populated state that corresponds to an unfolded ensemble. Exchange parameters that are in good agreement

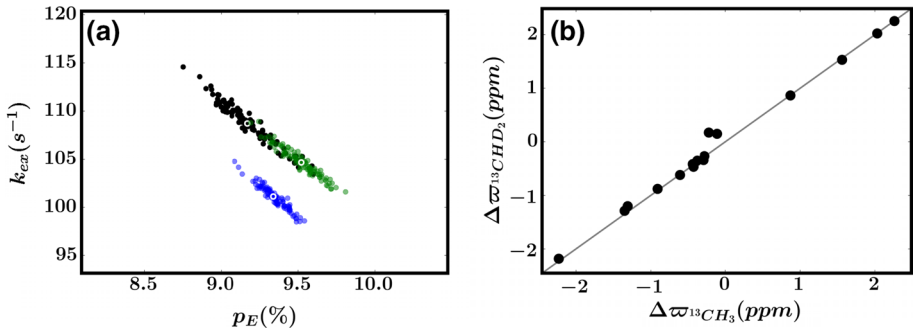

Fig. 6 **a** Distributions of fitted k_{ex} and p_E values from fits of CEST profiles recorded on the G48A Fyn SH3 domain, 25 °C, as described in "Materials and methods" section. Distributions were obtained from Monte Carlo analyses (Press et al. 1988) using the best-fit solutions to the experimental data and the experimentally determined intensity errors. Distributions calculated from fits of ^{15}N- (*black*) or $^{13}CHD_2$–CEST profiles without (*blue*) or with (*green*) ^{2}H decoupling are shown. **b** Linear correlation plot comparing ^{13}C $\Delta\varpi$ values obtained from analysis of CEST profiles recorded on $^{13}CH_3$- ($\Delta\varpi_{^{13}CH_3}$, (Bouvignies and Kay 2012)) and $^{13}CHD_2$ samples ($\Delta\varpi_{^{13}CHD_2}$, current study). The small deviations from the line for the two points with $\Delta\varpi \sim 0$ ($\Delta\varpi_{^{13}CHD_2} = 0.15$, 0.17 ppm and $\Delta\varpi_{^{13}CH_3} = -0.11$ and -0.22 ppm) reflect the difficulties in extracting highly accurate chemical shift differences when major and minor dips are extensively overlapped, as expected (Vallurupalli et al. 2012). *Error bars* in **b** are included, but are significantly smaller than the symbols

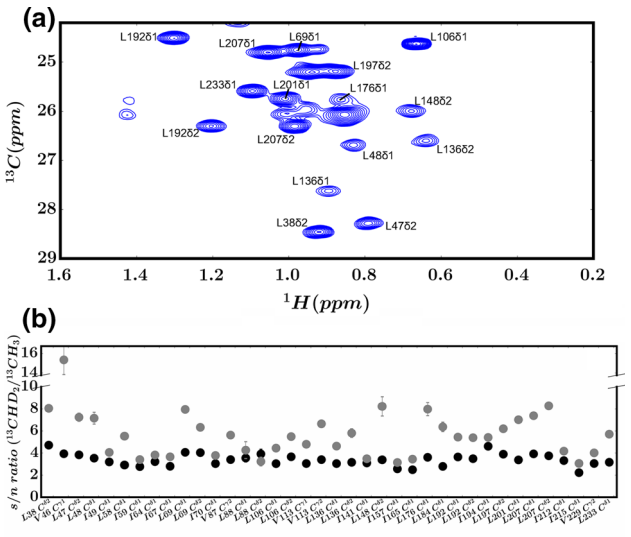

Fig. 7 **a** Selected region of the ^{13}C–^{1}H correlation map of [U-^{2}H; Ileδ1-$^{13}CHD_2$; Leu, Val-$^{13}CHD_2$/$^{13}CHD_2$; Met-$^{13}CH_3$]-$\alpha_7\alpha_7$ recorded with the sequence of Fig. 3, $T_{MIX} = 0$ s, 50 °C, 600 MHz. Assignments are as indicated. **b** s/n ratios for cross-peaks in $^{13}CHD_2$- versus $^{13}CH_3$–CEST, $T_{MIX} = 0$ s (*black*) and 0.5 s (*grey*), 50 °C

with those measured using ^{15}N-CEST experiments are obtained, validating the methodology. Substantial s/n improvements are noted with the $^{13}CHD_2$–CEST scheme over a $^{13}CH_3$-based experiment, even in applications to small proteins, with sensitivity gains over five fold, on average, in studies of the 360 kDa $\alpha_7\alpha_7$ complex. The significant advantages of $^{13}CHD_2$–CEST in this application make it clear that no single labeling scheme is optimal in all cases. Although $^{13}CH_3$ labeling has been shown to be the approach of choice in studies of high molecular weight proteins that can be carried out using HMQC-based experiments where a methyl-TROSY effect is operative, applications that involve the generation of pure ^{13}C magnetization are likely to benefit from $^{13}CHD_2$ labeling. In studies of large complexes such as molecular machines the sensitivity gains afforded by careful optimization of both labeling scheme and experiment may well prove to be essential.

Acknowledgments This work was supported by grants from the Canadian Institutes of Health Research and the Natural Sciences and Engineering Research Council of Canada. L.E.K holds a Canada Research Chair in Biochemistry.

Appendix: Effects of ^{2}H spin relaxation on $^{13}CHD_2$–CEST profiles

In a previous set of papers we have discussed the effects of homonuclear scalar couplings on CEST profiles and presented a simple approach for data analysis (Bouvignies et al. 2014; Vallurupalli and Kay 2013). By means of example, consider the case where ^{13}CO CEST profiles are obtained from measurements on a uniformly ^{13}C labeled protein sample. Each ^{13}CO dip is split into a doublet by the approximately 50 Hz ^{13}CO–$^{13}C^{\alpha}$ scalar coupling ($J_{C\alpha CO}$). Although multiplet components are generally not observed in ^{13}CO CEST profiles when weak B_1 fields on the order of 20 Hz or greater are used, the resultant dips are nevertheless broadened by the unresolved couplings and this effect should be taken into account in fits of the profiles to extract accurate exchange parameters. This can be most easily accomplished by solving the Bloch–McConnell equations (McConnell 1958) for two ^{13}CO lines, separated by $J_{C\alpha CO}$, that correspond to $^{13}C^{\alpha}$ spins in the up/down positions. Here it is assumed that the longitudinal relaxation of $^{13}C^{\alpha}$ is slow compared to the rate of exchange between conformers so that the resulting CEST profiles are the simple sum of a pair of profiles, one for $^{13}C^{\alpha}$

spin up and a second for $^{13}C^{\alpha}$ spin down. This procedure can be generalized when more than a single homonuclear coupling is present, as described previously (Bouvignies et al. 2014). The situation is more complex for $^{13}CHD_2$–CEST when ^2H decoupling is not used. In this case each ^{13}C dip is split into a 1:2:3:2:1 pentet structure from ^{13}C–^2H scalar coupling interactions. However, the ^2H spin flip rate cannot be assumed to be slow compared to the conformational exchange process, so that averaging of the multiplet components can occur simultaneously with chemical exchange, necessitating a more complex treatment. In what follows we assume that ^1H decoupling is employed during the CEST interval, as indicated in the pulse scheme of Fig. 3, and thus neglect the influence of the one bond ^1H–^{13}C scalar coupling.

The effects of ^2H spin flips on $^{13}CHD_2$ CEST profiles are best considered by first separating the methyl ^{13}C j magnetization $j \in \{x, y, z\}$ into distinct components according to the spin states of the pair of coupled deuterons. In what follows we consider initially a basis comprised of 6 operators, $L1_j$–$L6_j$, defined as,

$$\begin{aligned}
L1_j &= C_j[(1,1)] = 0.25C_j(D_{z,1}^2 + D_{z,1})(D_{z,2}^2 + D_{z,2}) \\
L2_j &= C_j[(1,0)+(0,1)] = 0.5C_j\{(D_{z,1}^2 + D_{z,1})(1 - D_{z,2}^2) \\
&\quad + (1 - D_{z,1}^2)(D_{z,2}^2 + D_{z,2})\} \\
L3_j &= C_j[(0,0)] = C_j\{(1 - D_{z,1}^2)(1 - D_{z,2}^2)\} \\
L4_j &= C_j[(1,-1)+(-1,1)] \\
&= 0.25C_j\{(D_{z,1}^2 + D_{z,1})(D_{z,2}^2 - D_{z,2}) \\
&\quad + (D_{z,1}^2 - D_{z,1})(D_{z,2}^2 + D_{z,2})\} \\
L5_j &= C_j[(-1,0)+(0,-1)] \\
&= 0.5C_j\{(D_{z,1}^2 - D_{z,1})(1 - D_{z,2}^2) \\
&\quad + (1 - D_{z,1}^2)(D_{z,2}^2 - D_{z,2})\} \\
L6_j &= C_j[(-1,-1)] = 0.25C_j(D_{z,1}^2 - D_{z,1})(D_{z,2}^2 - D_{z,2}).
\end{aligned} \tag{7}$$

In Eq. (7) $C_j[(A, B)]$ denotes the j component of ^{13}C magnetization coupled to ^2H spin 1 with magnetic quantum number A, $A \in (-1, 0, 1)$ and ^2H spin 2 with magnetic quantum number B, and $D_{z,k}$ is the z-component of magnetization from ^2H spin $k \in (1, 2)$. A straightforward, albeit lengthy, calculation shows that the relaxation of $L1_j$–$L6_j$, considering ^2H contributions and adding ^{13}C relaxation (R_1^C or R_2^C) in an ad hoc manner, is given by

$$\frac{d\vec{L}_j}{dt} = -\tilde{R}_j\vec{L}_j \tag{8}$$

where

$$\vec{L}_j = \{L1_j, L2_j, L3_j, L4_j, L5_j, L6_j\}^T \tag{9}$$

and

$$\tilde{R}_j = \begin{pmatrix}
-2\kappa_1-2\kappa_2-R_p^C & \kappa_1 & 0 & \kappa_2 & 0 & 0 \\
2\kappa_1 & -3\kappa_1-\kappa_2-R_p^C & 2\kappa_1 & \kappa_1 & \kappa_2 & 0 \\
0 & \kappa_1 & -4\kappa_1-R_p^C & 0 & \kappa_1 & 0 \\
2\kappa_2 & \kappa_1 & 0 & -2\kappa_1-2\kappa_2-R_p^C & \kappa_1 & 2\kappa_2 \\
0 & \kappa_2 & 2\kappa_1 & \kappa_1 & -3\kappa_1-\kappa_2-R_p^C & 2\kappa_1 \\
0 & 0 & 0 & \kappa_2 & \kappa_1 & -2\kappa_1-2\kappa_2-R_p^C
\end{pmatrix} \tag{10}$$

where the superscript T in Eq. (9) is the transpose operator,

$$\begin{aligned}
\kappa_1 &= \frac{6}{5}c^2J(\omega_D) \\
\kappa_2 &= \frac{12}{5}c^2J(2\omega_D),
\end{aligned} \tag{11}$$

$\frac{2c}{\pi} \sim 165$ kHz is the quadrupolar coupling constant and $J(\omega_D)$ is given by Eq. (2) of the main text. In Eq. (10) the value of p is 1 if $j = z$ (longitudinal relaxation) or 2 if $j \in \{x, y\}$ (transverse relaxation).

Eq. (8) is written in a basis where $j \in \{x, y, z\}$. The above equations can be 'expanded' by explicitly including terms for each of the x, y and z components so that the 6×6 $\tilde{R}$ matrix above ($\tilde{R}_6$) becomes an 18×18 matrix, $\tilde{R}_{18} = \tilde{I}_3 \otimes \tilde{R}_6$ where $\tilde{I}_3$ is a 3×3 identity matrix and $\vec{L} = \{L1_x, L2_x, L3_x, L4_x, L5_x, L6_x, \ldots, L6_z\}^T$. The effects of chemical shift and ^2H–^{13}C scalar-coupled evolution couple x and y components of magnetization and are included into matrix $\tilde{R}_{18}$ by noting that

$$\begin{aligned}
\frac{dC_x[(A,B)]}{dt} &= -(\omega + (A+B)2\pi J_{CD})C_y[(A,B)] \\
\frac{dC_y[(A,B)]}{dt} &= (\omega + (A+B)2\pi J_{CD})C_x[(A,B)]
\end{aligned} \tag{12}$$

Finally, two-site chemical exchange, $G \underset{k_{EG}}{\overset{k_{GE}}{\rightleftarrows}} E$, is taken into account (Allard et al. 1998; Helgstrand et al. 2000) by

a further expansion of the equations with $\vec{L} = \{L1_x^G, L2_x^G, L3_x^G, L4_x^G, L5_x^G, L6_x^G, \ldots, L6_z^G, L1_x^E \ldots, L6_z^E\}^T$

$$\tilde{R'}_{36} = \begin{pmatrix} \tilde{R}_{18}^G & \tilde{0}_{18} \\ \tilde{0}_{18} & \tilde{R}_{18}^E \end{pmatrix} + \begin{pmatrix} -k_{GE} & k_{EG} \\ k_{GE} & -k_{EG} \end{pmatrix} \otimes \tilde{I}_{18} \qquad (13)$$

where the superscripts G and E denote the ground and excited states and $\tilde{O}_{18}$ is an 18 dimensional null matrix. It is assumed that R_1^C values are identical in $\tilde{R}_{18}^G$ and $\tilde{R}_{18}^E$ but that corresponding spins in ground and excited states have distinct R_2^C rates. Software for fitting exchange data is available upon request.

References

Abragam A (1961) Principles of nuclear magnetism. Clarendon Press, Oxford

Allard P, Helgstrand M, Hard T (1998) The complete homogeneous master equation for a heteronuclear two-spin system in the basis of cartesian product operators. J Magn Reson 134:7–16

Ayala I, Sounier R, Use N, Gans P, Boisbouvier J (2009) An efficient protocol for the complete incorporation of methyl-protonated alanine in perdeuterated protein. J Biomol NMR 43:111–119

Bouvignies G, Kay LE (2012) A 2D (1)(3)C-CEST experiment for studying slowly exchanging protein systems using methyl probes: an application to protein folding. J Biomol NMR 53:303–310

Bouvignies G, Vallurupalli P, Kay LE (2014) Visualizing side chains of invisible protein conformers by solution NMR. J Mol Biol 426:763–774

Clore GM, Gronenborn AM (1991) Structures of larger proteins in solution: three- and four-dimensional heteronuclear NMR spectroscopy. Science 252:1390–1399

Fawzi NL, Ying J, Ghirlando R, Torchia DA, Clore GM (2011) Atomic-resolution dynamics on the surface of amyloid-beta protofibrils probed by solution NMR. Nature 480:268–272

Forsen S, Hoffman RA (1963) Study of moderately rapid chemical exchange reactions by means of nuclear magnetic double resonance. J Chem Phys 39:2892–2901

Gans P et al (2010) Stereospecific isotopic labeling of methyl groups for NMR spectroscopic studies of high molecular weight proteins. Angew Chem Int Ed 49:1958–1962

Gardner KH, Kay LE (1997) Production and incorporation of ^{15}N, ^{13}C, ^{2}H (^{1}H–δ1 methyl) isoleucine into proteins for multidimensional NMR studies. J Am Chem Soc 119:7599–7600

Gelis I et al (2007) Structural basis for signal-sequence recognition by the translocase motor SecA as determined by NMR. Cell 131:756–769

Goto NK, Kay LE (2000) New developments in isotope labeling strategies for protein solution NMR spectroscopy. Curr Opin Struct Biol 10:585–592

Goto NK, Gardner KH, Mueller GA, Willis RC, Kay LE (1999) A robust and cost-effective method for the production of Val, Leu, Ile (δ1) methyl-protonated ^{15}N-,^{13}C-,^{2}H-labeled proteins. J Biomol NMR 13:369–374

Grzesiek S, Anglister J, Ren H, Bax A (1993) 13C line narrowing by 2H decoupling in 2/13C/15N-enriched proteins. Applications to triple resonance 4D J-connectivity of sequential amides. J Am Chem Soc 115:4369–4370

Guenneugues M, Berthault P, Desvaux H (1999) A method for determining B1 field inhomogeneity. Are the biases assumed in heteronuclear relaxation experiments usually underestimated? J Magn Reson 136:118–126

Helgstrand M, Hard T, Allard P (2000) Simulations of NMR pulse sequences during equilibrium and non- equilibrium chemical exchange. J Biomol NMR 18:49–63

Huth JR, Bewley CA, Jackson BM, Hinnebusch AG, Clore GM, Gronenborn AM (1997) Design of an expression system for detecting folded protein domains and mapping macromolecular interactions by NMR. Protein Sci 6:2359–2364

Ikura M, Kay LE, Bax A (1990) A novel approach for sequential assignment of 1H, 13C, and 15N spectra of proteins: heteronuclear triple-resonance three-dimensional NMR spectroscopy. Appl Calmodulin Biochem 29:4659–4667

Isaacson RL, Simpson PJ, Liu M, Cota E, Zhang X, Freemont P, Matthews S (2007) A new labeling method for methyl transverse relaxation-optimized spectroscopy NMR spectra of alanine residues. J Am Chem Soc 129:15428–15429

Ishima R, Louis JM, Torchia DA (1999) Transverse C-13 relaxation of CHD2 methyl isotopomers to detect slow conformational changes of protein side chains. J Am Chem Soc 121:11589–11590

Kainosho M, Torizawa T, Iwashita Y, Terauchi T, Ono AM, Guntert P (2006) Optimal isotope labelling for NMR protein structure determinations. Nature 440:52–57

Kay LE, Torchia DA (1991) The effects of dipolar cross-correlation on ^{13}C methyl-carbon T_1, T_2 and NOE measurements in macromolecules. J Magn Reson 95:536–547

Kay LE, Ikura M, Tschudin R, Bax A (1990) Three-dimensional triple-resonance NMR spectroscopy of isotopically enriched proteins. J Magn Reson 89:496–514

Kay LE, Keifer P, Saarinen T (1992) Pure absorption gradient enhanced heteronuclear single quantum correlation spectroscopy with improved sensitivity. J Am Chem Soc 114:10663–10665

Korzhnev DM, Religa TL, Banachewicz W, Fersht AR, Kay LE (2010) A transient and low-populated protein-folding intermediate at atomic resolution Science 329:1312–1316

Levitt MH (1982) Symmetrical composite pulse sequences for NMR population-inversion. 2. Compensation of resonance offset. J Magn Reson 50:95–110

Lipari G, Szabo A (1982) Model-free approach to the interpretation of nuclear magnetic relaxation in macromolecules: 2. Analysis of experimental results. J Am Chem Soc 104:4559–4570

Lowe J, Stock D, Jap B, Zwickl P, Baumeister W, Huber R (1995) Crystal structure of the 20S proteasome from the archaeon *T. acidophilum* at 3.4 Å resolution. Science 268:533–539

McConnell HM (1958) Reaction rates by nuclear magnetic resonance. J Chem Phys 28:430–431

Messerlie BA, Wider W, Otting G, Weber C, Wuthrich K (1989) J Magn Reson 85:608–612

Nikonowicz EP, Sirr A, Legault P, Jucker FM, Baer LM, Pardi A (1992) Preparation of ^{13}C and ^{15}N labelled RNAs for heteronuclear multi-dimensional NMR studies. Nucl Acids Res 20:4507–4513

Ollerenshaw JE, Tugarinov V, Skrynnikov NR, Kay LE (2005) Comparison of $^{13}CH_3$, $^{13}CH_2D$, and $^{13}CHD_2$ methyl labeling strategies in proteins. J Biomol NMR 33:25–41

Palmer AG, Cavanagh J, Wright PE, Rance M (1991) Sensitivity improvement in proton-detected two-dimensional heteronuclear correlation NMR spectroscopy. J Magn Reson 93:151–170

Press WH, Flannery BP, Teukolsky SA, Vetterling WT (1988) Numerical recipes in C. Cambridge University Press, Cambridge

Religa TL, Kay LE (2010) Optimal methyl labeling for studies of supra-molecular systems. J Biomol NMR 47:163–169

Religa TL, Ruschak AM, Rosenzweig R, Kay LE (2011) Site-directed methyl group labeling as an NMR probe of structure and dynamics in supramolecular protein systems: applications to the proteasome and to the ClpP protease. J Am Chem Soc 133: 9063–9068

Rosenzweig R, Kay LE (2014) Bringing dynamic molecular machines into focus by methyl-TROSY NMR. Annu Rev Biochem 83:291–315

Ruschak AM, Kay LE (2009) Methyl groups as probes of supramolecular structure, dynamics and function. J Biomol NMR 46:75–87

Sattler M, Schleucher J, Griesinger C (1999) Heteronuclear multidimensional NMR experiments for the structure determination of proteins in solution employing pulsed field gradients. Prog Nucl Magn Reson Spectrosc 34:93–158

Schleucher J, Sattler M, Griesinger C (1993) Coherence selection by gradients without signal attenuation: application to the three-dimensional HNCO experiment. Angew Chem Int Ed Engl 32:1489–1491

Shaka AJ, Keeler J, Frenkiel T, Freeman R (1983) An improved sequence for broadband decoupling: WALTZ-16. J Magn Reson 52:335–338

Shaka AJ, Lee CJ, Pines A (1988) Iterative schemes for bilinear operators—application to spin decoupling. J Magn Reson 77:274–293

Sprangers R, Kay LE (2007) Quantitative dynamics and binding studies of the 20S proteasome by NMR. Nature 445:618–622

Tugarinov V, Kay LE (2004) An isotope labeling strategy for methyl TROSY spectroscopy. J Biomol NMR 28:165–172

Tugarinov V, Kay LE (2005a) Methyl groups as probes of structure and dynamics in NMR studies of high-molecular-weight proteins. ChemBioChem 6:1567–1577

Tugarinov V, Kay LE (2005b) Quantitative ^{13}C and ^{2}H NMR relaxation studies of the 723-residue enzyme malate synthase G reveal a dynamic binding interface. Biochemistry 44: 15970–15977

Tugarinov V, Hwang P, Ollerenshaw J, Kay LE (2003) Cross-correlated relaxation enhanced ^{1}H–^{13}C NMR spectroscopy of methyl groups in very high molecular weight proteins and protein complexes. J Am Chem Soc 125:10420–10428

Vallurupalli P, Kay LE (2013) Probing slow chemical exchange at carbonyl sites in proteins by chemical exchange saturation transfer NMR spectroscopy. Angew Chem Int Ed Engl 52: 4156–4159

Vallurupalli P, Bouvignies G, Kay LE (2012) Studying 'invisible' excited protein states in slow exchange with a major conformation. J Am Chem Soc 134:8148–8161

Velyvis A, Ruschak AM, Kay LE (2012) An economical method for production of (2)H, (13)CH_3-threonine for solution NMR studies of large protein complexes: application to the 670 kDa proteasome. PLoS One 7:e43725. doi:10.1371/journal.pone.0043725

Wang AC, Bax A (1993) Minimizing the effects of radio-frequency heating in multidimensional NMR experiments. J Biomol NMR 3:715–720

Werbelow LG, Grant DM (1977) Intramolecular dipolar relaxation in multispin systems. Adv Magn Reson 9:189–299

Werbelow LG, Marshall AG (1973) Internal rotation and nonexponential methyl nuclear relaxation for macromolecules. J Magn Reson 11:299–313

Yamazaki T, Lee W, Arrowsmith CH, Muhandiram DR, Kay LE (1994) A suite of triple resonance NMR experiments for the backbone assignment of ^{15}N, ^{13}C, ^{2}H labeled proteins with high sensitivity. J Am Chem Soc 116:11655–11666

Zhou JY, van Zijl PCM (2006) Chemical exchange saturation transfer imaging and spectroscopy. Prog Nucl Magn Reson Spectrosc 48:109–136